ORIGINAL RESEARCH ARTICLE

Effects of Remelting on the Properties of a Superelastic Cu–Al–Mn Shape Memory Alloy Fabricated by Laser Powder Bed Fusion

N. Babacan[1,2] · S. Pilz[1] · J. Hufenbach[1,3] · T. Gustmann[1,4]

Abstract Laser powder bed fusion (LPBF) constitutes a promising alternative to directly produce Cu-based shape memory parts with high superelasticity due to the fact that the grain size and morphology as well as the texture can be tailored during processing. It is known that immediate laser remelting of previously processed layers during LPBF can serve as an important and complementary method to improve part density and to adjust the microstructure and mechanical behavior. As a consequence, this study focuses on the effects of an additional remelting step on the material properties of an additively fabricated $Cu_{71.6}Al_{17.Mn_{11.4}}$ (at.%) shape memory alloy (SMA). Firstly, the effects of different remelting parameters, obtained via systematically changing the hatching distance and scanning speed, on the sample density and transformation temperatures were analyzed. Secondly, microstructural observations as well as incremental compression tests were performed to establish the relationships between the applied remelting process parameters, the microstructure, and the superelastic properties. The comparison of the results for remelted and non-remelted counterparts clearly proves that a subsequent exposure of already solidified layers can serve as an adaptive tool to improve the performance of Cu-based SMAs and to allow the fabrication of locally adapted shape memory parts for application-oriented scenarios.

Keywords Additive manufacturing · Laser powder bed fusion · Cu–Al–Mn shape memory alloy · Laser remelting · Martensitic transformation · Superelasticity

✉ N. Babacan
nazimbabacan@sivas.edu.tr

✉ T. Gustmann
t.gustmann@oscar-plt.de

1   Leibniz Institute for Solid State and Materials Research Dresden, Institute for Complex Materials, 01069 Dresden, Germany

2   Department of Mechanical Engineering, Sivas University of Science and Technology, 58100 Sivas, Turkey

3   Institute of Materials Science, Technische Universität Bergakademie Freiberg, Gustav-Zeuner-Str. 5, 09599 Freiberg, Germany

4   Present Address: OSCAR PLT GmbH, 01665 Klipphausen, Germany

Introduction

Laser powder bed fusion (LPBF) additive manufacturing technique is capable of directly fabricating high-performance near-net-shaped metallic structures [1] and it also allows to tailor geometrical [2] and microstructural [3] characteristics to some extent. Based on a 3D CAD model, LPBF processing constitutes a local and accurate melting of a supplied thin powder bed on a substrate plate which is repeated layer by layer. Conventionally available LPBF-processed alloys usually outperform their cast counterparts or exhibit promising mechanical properties in comparison to wrought materials [4]. However, challenges remain and still hinder a full industrial adaption of LPBF. There are only a limited number of qualified alloys, which are mostly structural [5]. Thus, emerging fields like the development

of additively manufactured intelligent and stimuli-responsive structures, so-called 4D printing [6], can only partially benefit from the given potential in additive manufacturing. 4D printing allows the fabrication of dynamic components which can adjust their shape, properties, or functionalities over time under predetermined external stimuli. Thus, the fourth dimension in the aforementioned terminology is mainly related to the stimuli-responsive characteristic of the additively manufactured geometry. Among metals, shape memory alloys (SMAs) are an important group of functional materials, and their unique mechanical behavior (shape memory effect, superelasticity) is of specific interest for a new generation of 4D-printed components [7].

LPBF of mainly NiTi-based [2, 8–14] and Cu-based [15–23] SMAs has gained remarkable interest, due to the ability to fabricate complex and functional as-built parts. This could pave the way for new applications in the medical and aerospace industries or enable better system integration (damping [24] and elastocaloric [25] purposes). In terms of both processing and superelastic properties at room temperature, ternary Cu–Al–Mn alloys have been considered a promising alternative to the popular NiTi-based alloys, owing to good printability and low costs [16, 26], large transformation strain [27], and high thermal conductivity [28]. However, the presence of grain constraints causes the inhibition of martensitic transformation in ordinary polycrystalline Cu–Al–Mn SMAs due to their highly anisotropic mechanical properties [29, 30]. Thus, local plastic deformation and functional degradation are inevitable for randomly textured and globular-grained microstructures [31]. Therefore, Cu–Al–Mn SMAs should be manufactured with a focus on obtaining a highly textured and bamboo-like or columnar-grained microstructure, in order to improve the superelasticity [32–35].

The advantage of being able to control the melt pool properties and solidification behavior during LPBF provides an excellent opportunity to create optimized microstructures by adjusting process parameters, such as laser power, hatching distance, layer thickness, or via fine-tuning the scanning strategy [23, 36–42]. For this reason, LPBF constitutes an important alternative to produce near-net-shape and high-quality Cu–Al–Mn parts with high superelasticity and without the need for applying additional post-processing steps. In a recent study, Babacan et al. [19] found the optimized laser power and hatching distance parameters for a constant 50-μm layer thickness value and spot size of about 90 μm through a comprehensive process study for $Cu_{71.6}Al_{17}Mn_{11.4}$ (at.%) SMA. Regardless of the energy input, the chemical composition results were quite close and unlike the castings, the rapid cooling after melting resulted in fully austenitic LPBF samples. In another study, the current authors [23] obtained approximately 6% recoverable strain under 8% compressive

applied strain as a result of incremental compression tests by optimizing the scan vector rotation angle in adjacent layers. It has also been found that no thermal post-treatment is required to obtain Cu–Al–Mn parts with pronounced superelasticity.

A promising and effective technique for further fine-tuning the part quality, microstructure, and corresponding mechanical behavior is the use of laser remelting [15, 17, 43–52]. Remelting is typically used as an in situ post-processing step of already molten and solidified areas during LPBF, which is also known as selective laser melting (SLM). In other words, it can serve as an additional tool to tailor the part quality (improving surface smoothness and sample density [15, 50]) as well as microstructure [53] and can be adopted to selected sample areas (applied locally, e.g., top or side surfaces) or the whole-specimen volume (applied to each layer). It is noteworthy that several researchers have studied the effect of an additional remelting step to optimize the material properties of NiTi [47, 54] and Cu–Al–Ni–Mn [15, 17] SMAs fabricated by LPBF. On the one hand, Bayati et al. [47] applied different remelting procedures by varying the laser power and scanning speed and found that a remelting step during LPBF processing of $Ni_{50.8}Ti_{49.2}$ (at.%) improves the surface roughness and density. Chmielewska et al. [54] have used elemental Ni and Ti powders to fabricate Ni–Ti parts via LPBF from blended feedstocks by applying different remelting strategies. In this study, remelting significantly reduced the sample porosity. Furthermore, the compositional homogeneity increased as the number of remelting steps per layer increased. However, this strategy could not completely eliminate the phase composition inhomogeneity and it was stated that further research is needed to fully understand the effects on the shape memory properties. On the other hand, Gustmann et al. [15, 17] investigated the influence of a remelting step (so-called selective laser remelting) on the relative density, microstructure, transformation temperatures, and mechanical properties of a quaternary Cu-11.85Al-3.2Ni-3Mn (wt.%) high-temperature SMA. The grain size evolution and transformation temperatures showed an increasing and comparable trend with increasing energy input during remelting, confirming general findings that have been reported for conventionally processed counterparts with different grain sizes [55]. In addition, the relative density, surface roughness, and the ductility (tensile test) were improved, while the mechanical properties under compressive stress have not drastically changed by remelting.

The studies described above demonstrate the general feasibility of adjusting the part and material properties of selected additively manufactured SMAs through an implemented remelting step. To the best of our knowledge, Cu–Al–Mn SMAs have not been prepared by LPBF and

remelting so far. We have previously demonstrated that Cu–Al–Mn parts with high density and columnar, single-phase microstructures as well as a pronounced superelasticity can be manufactured with optimized process parameters [19] and scanning strategies [23] by LPBF. In this article, we investigated an improvement of LPBF-manufactured $Cu_{71.6}Al_{17}Mn_{11.4}$ (at.%) parts by a subsequent remelting procedure of already processed layers to further decrease residual porosity and tailor the grain size as well as the texture. In a first step, a parameter study was conducted to establish suitable remelting parameters without negatively influencing the part density or surface roughness. In a second step, the interrelations between remelting, the resulting microstructures, and the mechanical performance have been revealed. The obtained findings demonstrate that an additional remelting step can be applied to fabricate as-built parts with high superelasticity and that individually developed post-scanning strategies facilitate a more flexible manipulation of different geometries and their local material behavior.

Experimental Procedure

Materials and Processing

In this study, cylindrical specimens (diameter: d_1 = 3 mm, d_2 = 5 mm, height = 11 mm) were fabricated under an argon atmosphere using a gas-atomized $Cu_{71.6}Al_{17}Mn_{11.4}$ (at.%) powder in a SLM 250^{HL} (SLM Solutions Group AG, Germany) device. A constant layer thickness of 50 μm and a bi-directional stripe scanning strategy were used during LPBF processing. A pre-heating of the substrate plate was not applied. The scan vector rotation between successive layers was held constant at 79°. As a consequence of our initial studies [19, 23], an optimized parameter setup with a laser power (P) of 325 W, scanning speed (v) of 1000 mm/s, and hatching distance (h) of 100 μm was chosen to produce crack-free samples with a minimum number of residual pores. The samples produced without remelting using these processing parameters were named as SLM-Ref as in [19].

The remelting process was varied using scanning speeds (v_r) of 500 to 1000 mm/s and hatching distances (h_r) of 50 to 90 μm (r: parameter indication, solely applied during remelting). The laser power (P_r) was kept constant (325 W) for every layer. In order to screen suitable process parameters for the immediate illumination of already solidified layers (remelting), an evaluation matrix of 5-mm-diameter cylindrical specimens was produced and analyzed via a digital confocal microscope (VHX-7000, Keyence Deutschland GmbH, Japan) in a first step (see Sect. "Selection of Process Parameters and Pore

Analysis"). In a second step, cylindrical specimens with diameters of 3 and 5 mm (height = 11 mm) were fabricated for material analysis (see Sect. "Sample Characterization") using selected remelting process parameters.

Sample Characterization

The density of remelted LPBF samples was obtained by the Archimedean method using an MSA 225S (Sartorius GmbH, Germany) device (three measurements in total per sample).

An X-ray computed tomography (μ-CT) device (Phoenix nanotom m, General Electric, USA) was used to analyze selected samples of 3 and 5 mm diameter for residual porosity (pore size and distribution). Before scanning, resolution and timing were set to 6 μm and 150 ms, respectively. To reduce scanning artifacts, all μ-CT scans were performed with a copper filter (0.3 mm thick). For each reconstruction of the sample volume, a total of 720 projections were recorded. The analysis of defects (e.g., equivalent pore diameter) was carried out using VG-Studiomax 2.2 (Volume Graphics GmbH, Germany) for a selected ISO-50 gray scale setting (applied gray-scale shift: ± 5 units). Pore diameters less than 15 μm (approximately 3 times the resolution limit/voxel size) were not included.

Differential scanning calorimetry (DSC) was employed to determine the transformation temperatures (TTs) of low-temperature aged samples (sample weight: 20 to 30 mg) at 200 °C for 30 min (see also [19, 23]). A DSC 8500 device (Perkin-Elmer, USA) was used to carry out the DSC analysis at heating and cooling rates of 10 °C/min.

The chemical compositions of the selected samples were analyzed using inductively coupled plasma-optical emission spectroscopy (ICP-OES; iCAP 6500 Duo View, Thermo Fisher Scientific, USA). The analysis involved a threefold solution-based approach.

For microstructural examinations, vibration-polished samples were examined by electron backscattered diffraction (EBSD) analyses. A scanning electron microscope (SEM; Gemini Leo 1530, Zeiss, Germany) equipped with a Bruker eFlash HR + (Bruker Nano, Germany) EBSD detector was used for these characterizations. The grain structure, crystalline orientation, and texture of the samples were compared. Further details on the sample preparation and EBSD measurements can be found in the preliminary work [23].

The superelastic properties were analyzed in compression using a 5869 universal testing machine (Instron Deutschland GmbH, Germany). A strain rate of 5×10^{-4} s^{-1} was maintained throughout the tests. The compressive strain was monitored using an AVE2 video extensometer (Instron). Manually ground co-planar as-built

compression test samples with 3 mm diameter and a height of 10 mm were used for the tests. Incremental loading–unloading tests up to 8% strain (1% step size) were performed on at least two specimens to reveal the superelastic properties of the specimens.

Results and Discussion

Selection of Process Parameters and Pore Analysis

The selection of suitable remelting parameters is of central importance for the investigation of the relationships between the applied remelting step, the resulting microstructure, and the shape memory behavior of additively produced $Cu_{71.6}Al_{17}Mn_{11.4}$. In analogy to process parameter studies, which are often used as a starting point to evaluate novel materials or fabrication strategies in LPBF, the scanning speed (v_r = 500 to 1000 mm/s) and hatching distance (h_r = 50 to 90 μm) were varied during remelting as seen in Fig. 1a. The focus of this approach was to identify parameter combinations which enable a stable processing for sample fabrication and to investigate if the layers were rather fully melted.

As implied in Fig. 1a, all the manufactured specimens were fully melted and no residual powder particles were found at the scanned top surfaces. The samples showed significant differences in the surface appearance with respect to the applied scanning speed. While the h_r-values were increased from top to bottom (row related: 1 to 5), the v_r values increased from left to right (column related: A to E). For relatively small scanning speeds (500 to 625 mm/s), the highest energy inputs (115 to 260 J/mm^3) and penetration depths resulted during remelting. Pronounced overheating and part distortion at the edges of the samples were observed irrespective of the applied hatching distance. Therefore, the fabrication of these samples was interrupted after approximately 10 applied powder layers and the relevant parameter combination were not further considered.

The higher the scanning speed, the smoother the sample surfaces appeared after processing (cf. Figure 1a columns C to E). It is noteworthy that the density of the samples C (7.243 to 7.342 g/cm^3) remained close to the value of the SLM-Ref sample (7.32 ± 0.01 g/cm^3 [19]) as seen in Table 1. An appropriate combination of scanning speed and hatching distance was used to both decrease the penetration depth during remelting [17] and produce specimens with no visible hotspots on the contours (v_r = 1000 mm/s). As a consequence, it is especially focused on the samples in column E for further tests. The high part quality in terms of the surface appearance was confirmed by Archimedean and precise μCT measurements as presented in Fig. 1b and

Table 1, respectively. For the latter, selected samples with the lowest (sample E1) and highest hatching distance (sample E5) were used and their results were additionally compared with the findings from μCT-scanned samples with 3 mm in diameter (Fig. 1c–e).

The μCT scans showed that crack-free LPBF samples with low residual porosity can be manufactured via remelting, irrespective of the investigated sample diameter or hatching distance. When the applied h_r-value is small, the majority of pores (equivalent diameter between 50 and 100 μm) concentrate near the contour of the 3 mm-diameter-samples. This was also observed for the 5-mm-diameter specimen. Please note that clustering of pores in Fig. 1c originates from a strong overlapping of detected voids due to the visualization. The number of pores (about 200 to 500) and the total volume porosity (approximately 0.005 to 0.03%) were found to be comparable to our previous findings [19, 23] and relatively low compared to other LPBF studies [56, 57]. However, a pronounced effect on the mechanical response, i.e., shape recovery, cannot be fully excluded at this point as stress concentrations in the areas close to the contour and, thus, local plastic deformation during superelastic cycling can occur [58]. Furthermore, a pronounced concentration of sub-millimeter defects in more filigree parts, e.g., thin walls, struts in open-porous geometries, needs to be monitored critically [2]. When the hatching is increased by a factor of 1.4 (h_r = 70 μm), the pore distribution becomes more homogenous, shifts to smaller values (equivalent diameters around 35 μm) and the number of pores further decreases (about 0.003 to 0.008% porosity). Similar results were recorded for the LPBF samples remelted with the highest hatching distance (h_r = 90 μm), whereas the defects in these samples was about twice as high.

On the basis of the optical images, a comparison of the density values and the pore analysis, representative LPBF specimens produced at a scanning speed of 1000 mm/s and the above-mentioned hatching distances (h_r: 50, 70, and 90 μm) were selected to produce test specimens for microstructural (Sect. "Influence of Remelting on the Microstructures and Transformation Behavior") and mechanical characterization (Sect. "Influence of the Remelting on the Superelastic Properties"). Throughout the paper, the selected specimens are referred to as H50 and H90, respectively. In addition, the results obtained by analyzing the SLM-Ref samples were used for comparison.

Influence of Remelting on the Microstructures and Transformation Behavior

Figure 2 presents the inverse pole figure (IPF) maps together with the grain (black) and subgrain (gray) boundaries of the SLM-fabricated samples along the BD
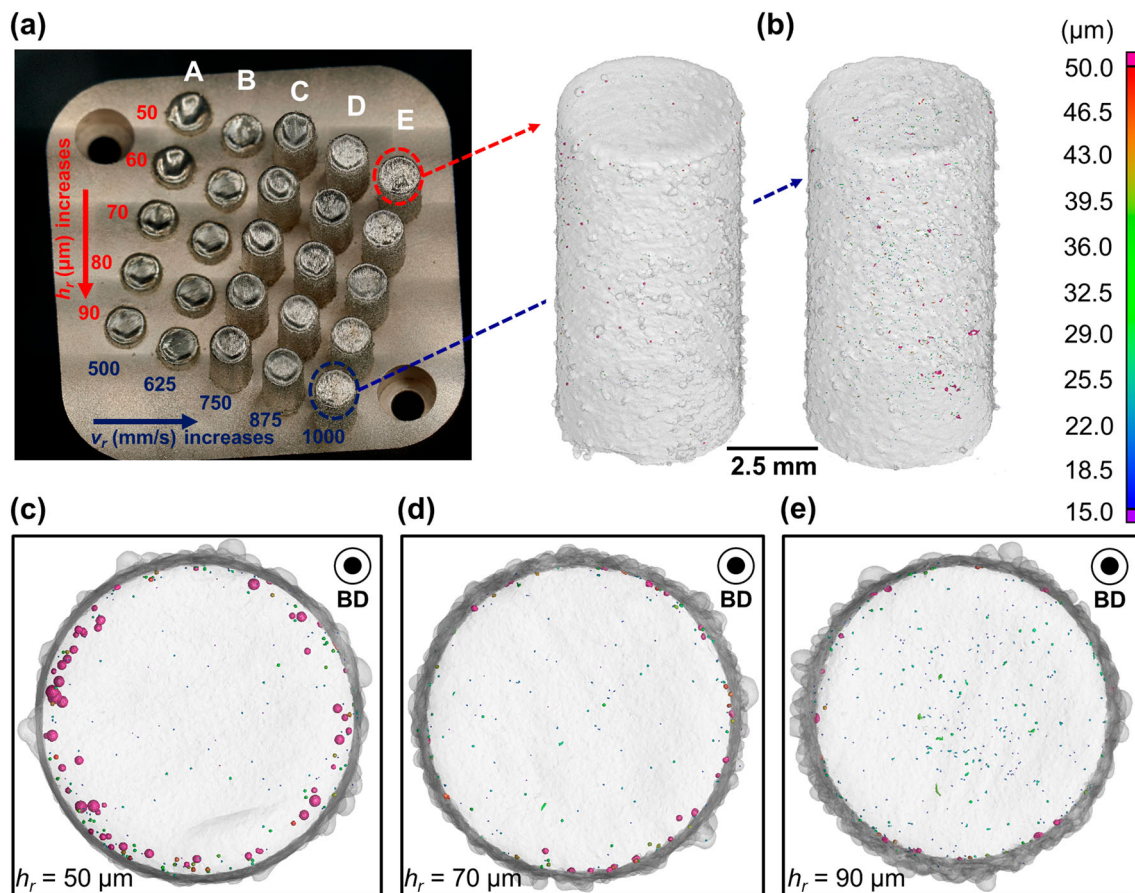
Fig. 1 a The macroscopic view of the LPBF samples (diameter = 5 mm, height = 11 mm) produced with different remelting processing parameters (P = 325 W, further parameters as implied in the image: v_r = 500 to 1000 mm/s, h_r = 50 to 90 μm). **b** The highlighted specimens in (**a**) were used for a detailed μCT analysis and are presented as reconstructed, transparent volumes. Visible pores and their equivalent diameters correspond to the shown scale bar. A μCT analysis of 3-mm-diameter samples produced with h_r-values of **c** 50 μm (227 voids, porosity = 0.03 ± 0.002%), **d** 70 μm (215 voids, porosity = 0.008 ± 0.002%), and **e** 90 μm (443 voids, porosity = 0.01 ± 0.001%) is shown as comparison (top view) (Color figure online)

(building direction) and perpendicular to the BD. A minimum misorientation angle of 15° was defined as the threshold value grain boundaries and 5° for subgrain boundaries. All samples have a fully austenitic (L2₁) microstructure and consist of columnar grains with a strong {100} texture along BD and a high amount of subgrains (Fig. 2a–c). The average intercept lengths in X- and Y-directions were calculated from the defined subsets in Fig. 2d–f for the 15° minimum grain boundary threshold value and the results are tabulated in Table 2.

The intercept lengths of the remelted samples in both directions are higher than those of the non-remelted sample. Song et al. [48] and Bedmar et al. [59] also found that remelting coarsened the grain sizes of the 18Ni-300 maraging steel and Ti6Al4V samples, respectively. In addition, the intercept lengths become wider when higher energy input is applied during remelting similar to the study of Gustmann et al. [17] for Cu–Al–Ni–Mn SMAs. The remelting strategy results in a higher melt pool

temperature due to the additional energy input and therefore, the cooling rate of the melt pool might be lower compared to non-remelted specimens, resulting in grain coarsening by remelting [60]. Thus, a higher energy input during remelting promotes this phenomenon and grain coarsening becomes more dominant.

It is known that reducing the misorientation between grains of Cu-based SMAs improves the compatibility of phase transformation, weakens the grain boundary constraints, and reduces the stress concentrations at triple junctions, which helps to increase the superelastic performance [61]. Therefore, the (sub)grain boundary misorientation angle distribution histogram for remelted H50 and H90 samples, as well as SLM-Ref measured for cross-sections perpendicular to the BD is plotted and presented in Fig. 3. It appears that remelting not only causes larger grains to form a higher proportion, but also produces grains with smaller misorientation angles. Larger misorientations in the SLM-Ref sample could lead to a higher

Table 1 Overview of remelted LPBF samples (remelting parameters, v_r: scanning speed, h_r: hatching distance, E_r: Energy input) as further indicated in Fig. 1a. The process parameters of the samples E1, E3, and E5 were chosen for the manufacturing of specimens for further analysis. The applied laser power, P_r, was held constant at 325 W. 3D-reconstructed volumes of the samples E1 and E5 are presented in Fig. 1b

| Sample ID	v_r (mm/s)	h_r (µm)	E_r (J/mm³)	Density (g/cm³)	µCT results Porosity (%)	Amount of pores
C1	750	50	173.3	7.301 ± 0.005	–	
C2		60	144.4	7.257 ± 0.004		
C3		70	123.8	7.243 ± 0.007		
C4		80	108.3	7.303 ± 0.003		
C5		90	96.3	7.342 ± 0.01		
D1	875	50	148.6	7.339 ± 0.003		
D2		60	123.8	7.345 ± 0.002		
D3		70	106.1	7.348 ± 0.002		
D4		80	92.9	7.354 ± 0.004		
D5		90	82.5	7.356 ± 0.003		
E1	1000	50	130.0	7.357 ± 0.001	0.005 ± 0.002	461
E2		60	108.3	7.362 ± 0.003	–	
E3		70	92.9	7.358 ± 0.001	0.003 ± 0.001	498
E4		80	81.3	7.357 ± 0.007	–	
E5		90	72.2	7.361 ± 0.004	0.010 ± 0.006	1140
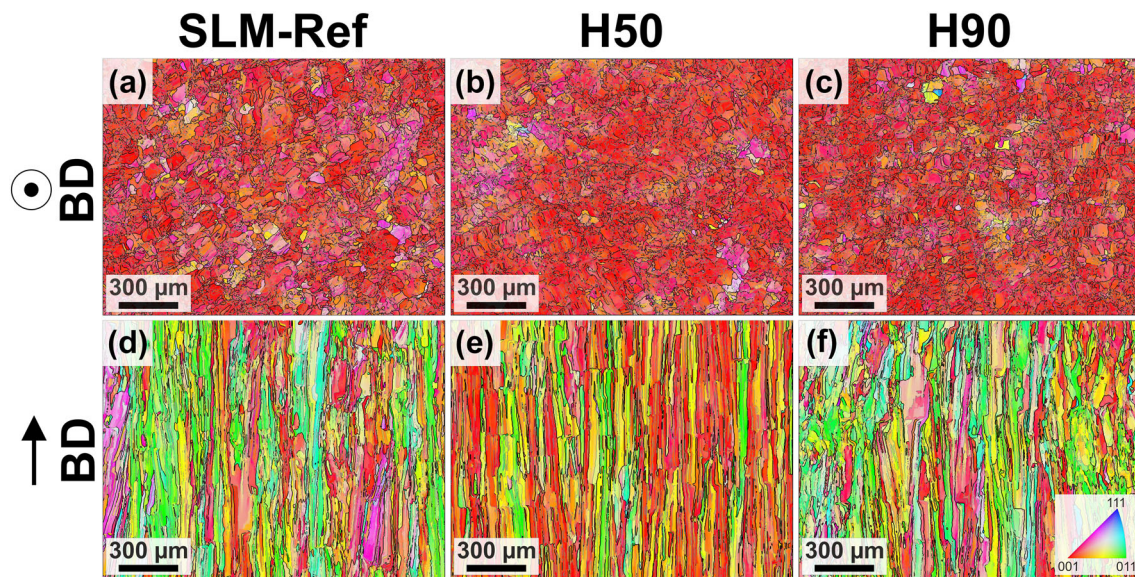
Fig. 2 Inverse pole figure maps of **a**, **d** SLM-Ref, **b**, **e** H50, and **c**, **f** H90 samples: **a–c** perpendicular to BD and **d–f** along BD. The color coding is given with respect to normal direction of the sample surface. Grain boundaries (> 15° misorientation) are marked by black and subgrain boundaries (5–15°) are marked by gray lines (Color figure online)

Table 2 Grain intercept lengths correspond to the EBSD analysis of subset in Fig. 2d–f (perpendicular to BD) (E: volumetric energy input)

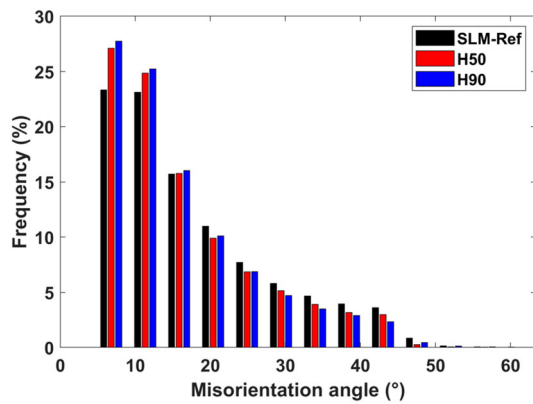| Sample	E (J/mm³) Initial melting	Remelting	Minimum grain boundary threshold = 15° Intercept length (X) (µm)	Intercept length (Y) (µm)
SLM-Ref	65	–	84	80
H50	65	130	149	129
H90	65	72	127	113

Fig. 3 Grain boundary misorientation angle distributions of selected subsets from the EBSD analysis in Fig. 2d–f (perpendicular to BD) (Color figure online)
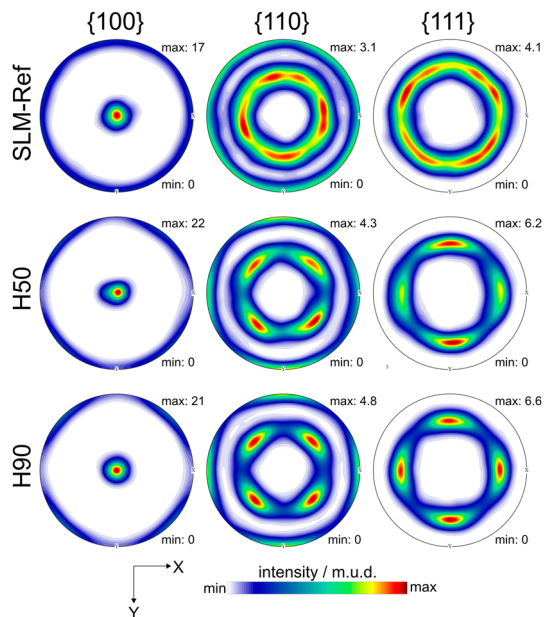

Fig. 4 {100}, {110}, and {111} pole figures of the analyzed areas in Fig. 2d–f for SLM-Ref, H50, and H90 specimens, respectively (Color figure online)

heterogeneous nucleation rate which will result in smaller grains, consistent with the finding in Fig. 2 and Table 2 [62]. Besides, it is observed that the relative frequency of low angle grain boundaries slightly increases with increasing the hatching distance during remelting.

The pole figures derived from the EBSD measurements Fig. 2d–f are given in Fig. 4. All samples show a pronounced {100} texture along the BD due to the alignment of the preferred growth direction (< 100 >) with the direction of the heat flow during manufacturing. For both hatching distances discussed, the remelting step leads to a slight increase of the {001} texture strength along the BD. For the SLM-Ref sample a clear < 100 > fiber texture along BD is visible leading to a nearly homogeneous

distribution of the {100} orientation density in the X–Y plane and the ring-like orientation density distributions for the {110} and {111} pole figures.

In contrast to the non-remelted sample, the fiber texture of the remelted counterparts (H50, H90) changes to a more single crystal-like cube texture with distinct spots of the orientation density in the different pole figures. Therefore, an increase of the hatching distance from 50 to 90 μm creates a more pronounced single crystal-like texture with sharper intensity peaks. This trend is also supported by Fig. 5, illustrating the area belonging to the strongest texture component (up to a maximum misorientation of 15°), which is 25% for the SLM-Ref sample. Remelting significantly increases its fraction to around 34 and 42% for the samples H50 and H90, respectively.

Remelted samples produced with 1000-mm/s scanning speed and varying hatching distances were aged at 200 °C for 30 min and their transformation temperatures (TTs) were compared by means of DSC analysis. It is already known from the previous study [23] that the forward martensitic TTs of the as-built SLM-Ref sample are below − 80 °C. Due to the fact that these temperatures are beyond the cooling capacity limit of the DSC instrument used in this study, the low-temperature aging procedure, which is known to increase the TTs in Cu–Al–Mn SMAs [63], was utilized to fully monitor the TTs of the samples. The same aging treatment applied to all samples can be considered negligible for the comparison of transformation behavior.

The 2nd-cycle DSC curves of the low-temperature aged samples are shown in Fig. 6. All remelted samples exhibited higher TTs compared to SLM-Ref sample. Besides, an increasing trend in TTs is obtained with decreasing the hatching distance. Therefore, TTs tend to rise with remelting and the volumetric energy input value during the remelting can shift the TTs. Grain size, which depends on the energy density in LPBF and might dominate over TTs in Cu-based SMAs [64], could play a key factor in this result. As seen in Table 2, the grain intercept lengths of the remelted samples are higher than those of the SLM-Ref sample. In addition, the H50 sample has higher intercept lengths compared to the H90 sample. Thus, the shift of TTs to higher values could be attributed to grain coarsening as a result of increased energy input.

Furthermore, an important obstacle encountered in the LPBF of certain alloys is the potential evaporation of specific elements during the process (very high local temperatures), primarily due to their high vapor pressure in the molten state. Mn is one of those elements that can be evaporated during processing as seen in several studies [65–67]. To better clarify if there is an influence of the remelting procedure on the Mn content and, thus, on the TTs, the chemical compositions of selected H50 and H90
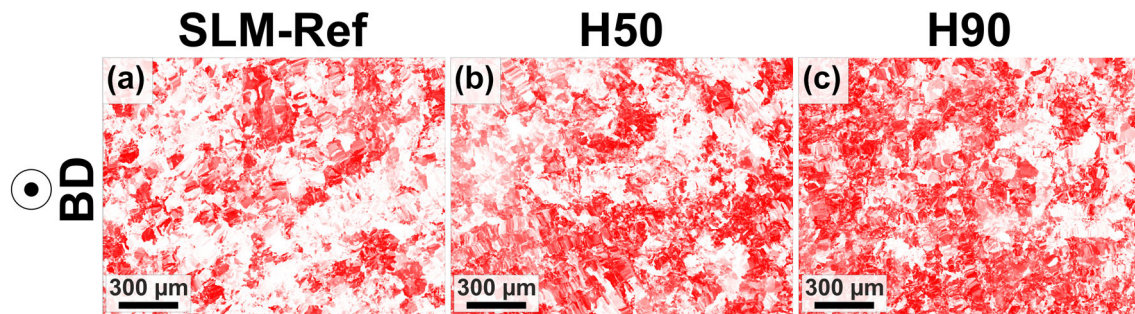
SLM-Ref   H50   H90

Fig. 5 EBSD maps of the areas belonging to the strongest texture component (max. misorientation 15°) of **a** SLM-Ref, **b** H50, and **c** H90 samples (Color figure online)
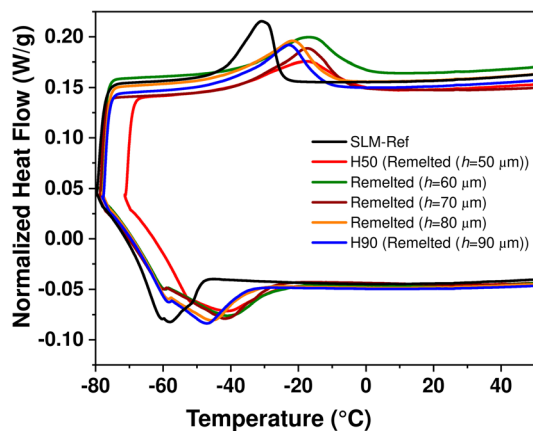

Fig. 6 Comparison of the transformation behavior in case of second-cycle DSC curves of aged remelted specimens and a non-remelted counterpart. The DSC curve of the latter sample was reproduced and found to be similar to the previous results [19] (Color figure online)

Table 3 Experimental determined chemical compositions and corresponding relative standard deviations of the SLM-Ref, H50, and H90 samples

	Cu (at.%)	Al (at.%)	Mn (at.%)
SLM-Ref	72.00 ± 0.38	16.87 ± 0.10	11.13 ± 0.08
H50	72.13 ± 0.48	16.97 ± 0.06	10.90 ± 0.06
H90	72.02 ± 0.46	16.99 ± 0.06	10.99 ± 0.06

Influence of the Remelting on the Superelastic Properties

The superelastic properties of the remelted and SLM-Ref samples were characterized by incremental compression tests and the resulting stress–strain curves and recoverability of the samples are shown in Fig. 7. For simplicity, only one stress–strain curve from each condition is shown. It can be seen that shape recovery increases by remelting and a higher maximum recoverable strain ($4.81 \pm 0.18\%$) was obtained in the H90 sample compared to the H50 ($4.03 \pm 0.05\%$) and SLM-Ref ($3.73 \pm 0.07\%$) specimens (Fig. 7b). Although the recoverable strain of the H90 sample increased up to 8% applied strain, it began to decrease for the H50 and SLM-Ref samples at the 8th loading step (corresponding to 8% applied strain). In addition to these three conditions examined in this study, the superelasticity test results of the sample 90° [23], in which all production parameters are identical to the SLM-Ref except that the scan vector rotation was 90° instead of 79°, were added for comparison. These samples exhibited a maximum recoverable strain of $5.60 \pm 0.03\%$, which was superior to even the remelted samples.

One of the key factors affecting the superelastic behavior of the Cu–Al–Mn SMAs is the grain misorientation. When the grains have different orientations, the increase in anisotropy in the microstructure usually results in a deterioration of the shape recovery. Large misorientations lead to increased dislocation pile-up across the grain
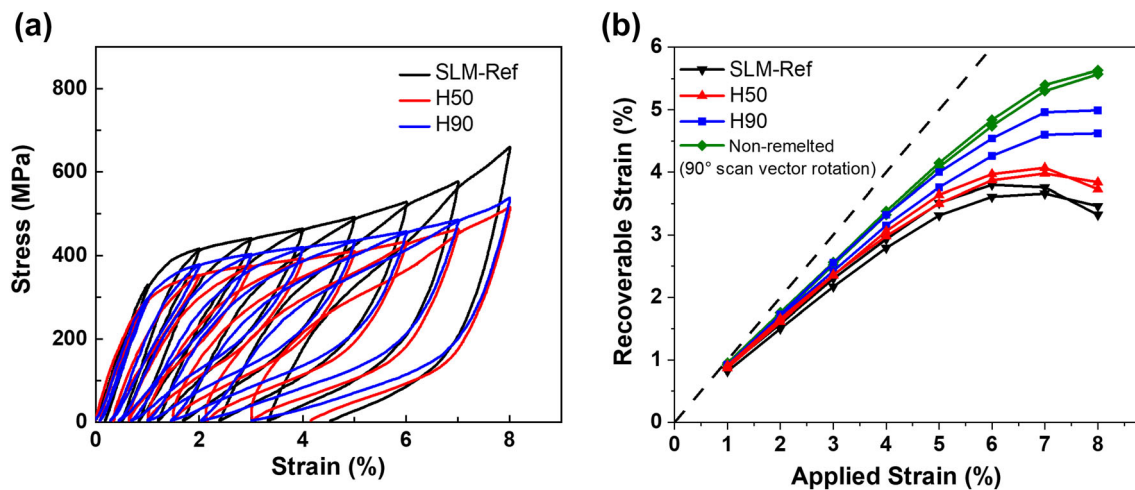
specimens were analyzed and compared to the findings of the non-remelted sample state (see Table 3).

In our previous publication ([19]), an elemental loss during processing irrespective of the energy input (55 to 133 J/mm³) has not been observed. If remelting is applied, it is seen that the Mn content slightly decreases. The H50 sample, subjected to higher energy inputs during remelting, exhibited a slightly greater loss of Mn (10.90 ± 0.06 at.%) compared to the H90 sample (10.99 ± 0.06 at.%). Consequently, the alteration in the chemical composition of the elements can be considered as an influencing factor of the TT shift which is further facilitated by the literature [68, 69]. However, due to the fact that the changes in the Mn content with respect to the non-remelted counterpart remain very small (cf. deviation values in Table 3), it does appear that these findings, also in comparison with the shift of the grain sizes due to remelting, are not the dominating factor for the increase of the TTs.

Fig. 7 a Incremental compressive stress–strain curves of as-built SLM-Ref (non-remelted reference sample) and remelted (H50 and H90) LPBF specimens tested at room temperature. Only results from a selected sample were plotted. **b** Recoverable strain versus applied strain. The values were extracted from the recorded stress–strain curves for two samples each. The solid-dashed line illustrates full strain recovery condition. The results of the as-built samples that were produced with 90° scan vector rotation instead of 79° (see [23]) were added for comparison (Color figure online)

boundary and thus plastic deformation, which reduces the recoverability of SMAs [61]. In addition, as the grain size of the parent phase decreases in Cu–Al-based systems, the recoverable strain decreases due to grain boundary constraints [70]. In other words, the shift of the misorientation distribution to higher angle values and the relatively small grain sizes in the SLM-Ref sample (cf. Fig 3 and Table 2), respectively, are one of the governing factors why this sample shows a poor superelastic performance compared to the counterparts. Moreover, the higher value of the stress-induced martensitic transformation slope, which corresponds to the work-hardening rate, observed for the SLM-Ref sample in Fig. 7a, is an indication of the higher accumulation of dislocation slips. Similarly, the critical stress of the stress-induced martensitic transformation, which is strongly dependent on grain size and grain boundary constraints [71], shows the opposite tendency with recoverable strain and typically, the critical stress decreases with increasing grain size [72].

The texture discrepancy could be used to explain the difference in superelastic properties between remelted samples with different hatching distances. The remelting process results in a transition from fiber to a single crystal-like cubic texture, reducing mechanical constraints. Moreover, compared to H50, H90 has a sharper intensity peak with a more single crystal-like texture, which promotes the mechanical performance in terms of superelastic performance. As stated in Sect. "Selection of Process Parameters and Pore Analysis," an additional influence of the number of pores and pore concentration close to the surface (cf. Fig 1c–e) can be detrimental to the shape recovery under cycling conditions. As this is beyond the

scope of the present work, possible effects of residual porosity (e.g., non-machined with post-machined as-built specimens) on the shape recovery and local strain concentration will be subjected to upcoming investigations.

Conclusion

In this work, a direct remelting of already solidified layers during laser powder bed fusion of a $Cu_{71.6}Al_{17}Mn_{11.4}$ (at.%) shape memory alloy has been applied to study the effects on the part density, microstructure, and superelastic behavior. A set of different samples with varying scanning speeds (500 to 1000 mm/s) and hatching distances (50 to 90 µm) were manufactured and the results (e.g., transformation temperatures, superelastic properties) for selected samples were investigated in comparison to reference samples of our previous studies [19, 23]. The following conclusions can be drawn from the obtained findings:

1. Negligible differences in the density of different remelted samples revealed that additional post-scanning with parameters close to the evaluated process window (e.g., constant laser power) during LPBF can be efficiently used to tailor superelastic properties.

2. Remelting of Cu–Al–Mn to ultimately increase part density has to be carried out with higher scanning speeds (v_r = 750 to 1000 mm/s) and, thus, lower energy inputs (E_r = 72.2 to 173.3 J/mm^3). A hatching distance between a low track overlap (hatching close to the LPBF process value, 100 µm) and high track overlap criteria (50% less hatching with respect to the LPBF process value) led to specimens with the lowest

residual porosity and a reduced pore formation in the contour areas ($P_r = 325$ W, $v_r = 1000$ mm/s, $h_r = 70$ µm).

3. The measured intercept lengths revealed that the additional remelting step causes a significant shift of the grain sizes to higher values in contrast to non-remelted counterparts. While lower energy inputs and less hatching vectors ($E_r = 72.2$ J/mm^3, $h_r = 90$ µm) showed an enhancement of around 40 to 50%, the grain sizes further increased when more hatching vectors were applied ($E_r = 130.0$ J/mm^3, $h_r = 50$ µm). In other words, remelting remarkably coarsened the microstructure. Furthermore, a small amount of Mn evaporation was observed if remelting, particularly at higher energy inputs, were applied. However, it is believed that the slight alteration of the chemical composition is not the dominating factor for the shift of the transformation temperatures.

4. A detailed EBSD and texture analysis revealed that remelting leads to a shift of the grain boundary misorientation angle distribution to lower values and supports the formation of a single crystal-like texture. Thus, the microstructure of a non-remelted SLM-Ref sample (79° scan vector rotation) holds pronounced constraints for a shape recovery after loading/ unloading. Besides, the remelted sample produced with a 90 µm hatching distance showed a higher texture intensity, which further promotes the recoverable strain compared to the specimen manufactured with a 50 µm hatching distance.

5. An improvement in superelasticity was obtained via remelting with adjusted hatching distances, demonstrating the impact not only on the microstructure but also on the mechanical properties. In contrast to the non-remelted SLM-Ref sample produced with 79° scan vector rotation (about 3.7%), the compressive superelasticity of the remelted counterparts (about 4.8%) under incremental strain was found to be higher.

6. In general, it was demonstrated that achieving high superelasticity in Cu-Al-Mn parts produced by LPBF does not necessitate thermal or mechanical post-processing. This conclusion is supported by the highest recorded recoverable strain values of approximately 5.6% obtained from as-built Cu–Al–Mn parts, through the optimization of the scan vector rotation [23], as well as the findings from this study with respect to the remelting procedure.

The results of this work represent a promising way to fabricate near-net-shape Cu–Al–Mn shape memory parts with high recoverable strains in the as-built condition without making major changes to the evaluated processing conditions. Unlike the scanning strategy adjustments, a remelting procedure can be flexibly applied to existing LPBF scenarios in which process parameters have been optimized for specific part designs or build-job configurations. We believe that the findings of this study can be used for the manufacturing of more complex shape memory parts (e.g., lattices, grippers) with locally adjusted properties. Due to the fact that a post-scanning during LPBF can be easily applied to any layer (or material) and allows microstructural changes (texture, grain size) without negatively influencing the chemical composition, it offers unique possibilities for shape memory alloy design. Applying mechanical or thermal post-processing is usually not required but can still be involved after manufacturing to further adjust the material behavior (transformation temperature, shape recovery). This together allows for a better adoption of 4D printing of functional materials, across different disciplines as a resource-efficient fabrication route for the future.

Author Contributions NB participated in the Conceptualization, Methodology, Investigation, Visualization, Writing of the original draft, and Writing, reviewing, & editing of the manuscript. SP participated in the Investigation, Methodology, and Writing, reviewing, & editing of the manuscript. JH contributed to Resources and Writing, reviewing, & editing of the manuscript. TG participated in the Conceptualization, Methodology, Investigation, Visualization, Writing of the original draft, and Writing, reviewing, & editing of the manuscript.

Data Availability The data supporting the findings of this study are available from the corresponding authors on reasonable request.

Competing interest The authors declare that they have no known competing financial interests or personal relationships that could have appeared to influence the work reported in this paper.

References

1. Gu D, Shi X, Poprawe R, Bourell DL, Setchi R, Zhu J (2021) Material-structure-performance integrated laser-metal additive manufacturing. Science. https://doi.org/10.1126/science.abg1487

2. Gustmann T, Gutmann F, Wenz F et al (2020) Properties of a superelastic NiTi shape memory alloy using laser powder bed fusion and adaptive scanning strategies. Prog Addit Manuf 5:11–18. https://doi.org/10.1007/s40964-020-00118-6

3. Yasa E, Kruth JP, Deckers J (2011) Manufacturing by combining selective laser melting and selective laser erosion/laser re-melting. CIRP Ann Manuf Technol 60:263–266. https://doi.org/10.1016/j.cirp.2011.03.063

4. Narasimharaju SR, Zeng W, See TL et al (2022) A comprehensive review on laser powder bed fusion of steels: processing,

microstructure, defects and control methods, mechanical properties, current challenges and future trends. J Manuf Process 75:375–414. https://doi.org/10.1016/j.jmapro.2021.12.033

5. Blakey-Milner B, Gradl P, Snedden G et al (2021) Metal additive manufacturing in aerospace: a review. Mater Des 209:110008. https://doi.org/10.1016/j.matdes.2021.110008

6. Lu HZ, Yang C, Luo X et al (2019) Ultrahigh-performance TiNi shape memory alloy by 4D printing. Mater Sci Eng A 763:138166. https://doi.org/10.1016/j.msea.2019.138166

7. Zhou K (2022) Additive manufacturing: materials, functionalities and applications, 1st edn. Springer, Cham

8. Ma J, Franco B, Tapia G et al (2017) Spatial control of functional response in 4D-printed active metallic structures. Sci Rep 7:1–8. https://doi.org/10.1038/srep46707

9. Wang X, Kustov S, Van Humbeeck J (2018) A short review on the microstructure, transformation behavior and functional properties of NiTi shape memory alloys fabricated by selective laser melting. Materials (Basel) 11:1683. https://doi.org/10.3390/ma11091683

10. Nematollahi M, Toker G, Saghaian SE et al (2019) Additive manufacturing of Ni-rich NiTiHf20: manufacturability, composition, density, and transformation behavior. Shape Mem Superelasticity 5:113–124. https://doi.org/10.1007/s40830-019-00214-9

11. Farjam N, Nematollahi M, Andani MT et al (2020) Effects of size and geometry on the thermomechanical properties of additively manufactured NiTi shape memory alloy. Int J Adv Manuf Technol 107:3145–3154. https://doi.org/10.1007/s00170-020-05071-w

12. Alberto C, Jacopo B, Fabrizio F et al (2020) Selective laser melting of NiTi shape memory alloy: processability, microstructure, and superelasticity. Shape Mem Superelasticity. https://doi.org/10.1007/s40830-020-00298-8

13. Xue L, Atli KC, Zhang C et al (2022) Laser powder bed fusion of defect-free NiTi shape memory alloy parts with superior tensile superelasticity. Acta Mater 229:117781. https://doi.org/10.1016/j.actamat.2022.117781

14. Straub T, Fell J, Zabler S et al (2023) Characterization of filigree additively manufactured NiTi structures using micro tomography and micromechanical testing for metamaterial material models. Materials (Basel) 16:676. https://doi.org/10.3390/ma16020676

15. Gustmann T, Neves A, Kühn U et al (2016) Influence of processing parameters on the fabrication of a Cu–Al–Ni–Mn shape-memory alloy by selective laser melting. Addit Manuf 11:23–31. https://doi.org/10.1016/j.addma.2016.04.003

16. Gustmann T, dos Santos JM, Kühn U et al (2016) Properties of Cu-based shape-memory alloys prepared by selective laser melting. Shape Mem Superelasticity 3:24–36. https://doi.org/10.1007/s40830-016-0088-6

17. Gustmann T, Schwab H, Kühn U, Pauly S (2018) Selective laser remelting of an additively manufactured Cu–Al–Ni–Mn shape-memory alloy. Mater Des 153:129–138. https://doi.org/10.1016/j.matdes.2018.05.010

18. Tian J, Zhu W, Wei Q et al (2019) Process optimization, microstructures and mechanical properties of a Cu-based shape memory alloy fabricated by selective laser melting. J Alloys Compd 785:754–764. https://doi.org/10.1016/j.jallcom.2019.01.153

19. Babacan N, Pauly S, Gustmann T (2021) Laser powder bed fusion of a superelastic Cu–Al–Mn shape memory alloy. Mater Des 203:109625. https://doi.org/10.1016/j.matdes.2021.109625

20. Pérez-cerrato M, Fraile I, Gómez-cortés JF et al (2022) Designing for shape memory in additive manufacturing of Cu–Al–Ni shape designing for shape memory alloy processed by laser powder bed fusion. Materials (Basel) 15:6284. https://doi.org/10.3390/ma15186284

21. Mazzer EM, Kiminami CS, Gargarella P et al (2014) Atomization and selective laser melting of a Cu–Al–Ni–Mn shape memory alloy. Mater Sci Forum 802:343–348. https://doi.org/10.4028/www.scientific.net/MSF.802.343

22. Gargarella P, Mazzer EM, Basilio LA et al (2015) Phase formation, thermal stability and mechanical properties of a Cu–Al–Ni–Mn shape memory alloy prepared by selective laser melting. Mater Res 18:35–38. https://doi.org/10.1590/1516-1439.338914

23. Babacan N, Pilz S, Pauly S et al (2023) Tailoring the superelastic properties of an additively manufactured Cu–Al–Mn shape memory alloy via adjusting the scanning strategy. Mater Sci Eng A 862:144412. https://doi.org/10.1016/j.msea.2022.144412

24. Mazzer EM, da Silva MR, Gargarella P (2022) Revisiting Cu-based shape memory alloys: recent developments and new perspectives. J Mater Res 37:162–182. https://doi.org/10.1557/s43578-021-00444-7

25. Hou H, Simsek E, Stasak D et al (2017) Elastocaloric cooling of additive manufactured shape memory alloys with large latent heat. J Phys D Appl Phys 50:3–6. https://doi.org/10.1088/1361-6463/aa85bf

26. Alagha AN, Hussain S, Zaki W (2021) Additive manufacturing of shape memory alloys: a review with emphasis on powder bed systems. Mater Des 204:109654. https://doi.org/10.1016/j.matdes.2021.109654

27. Sutou Y, Omori T, Wang JJ et al (2004) Characteristics of Cu–Al–Mn-based shape memory alloys and their applications. Mater Sci Eng A 378:278–282. https://doi.org/10.1016/j.msea.2003.12.048

28. Wang H, Huang H, Xie J (2017) Effects of strain rate and measuring temperature on the elastocaloric cooling in a columnar-grained $Cu_{71}Al_{17.5}Mn_{11.5}$ shape memory alloy. Metals (Basel) 7:527. https://doi.org/10.3390/met7120527

29. Lu NH, Chen CH (2021) Inhomogeneous martensitic transformation behavior and elastocaloric effect in a bicrystal Cu–Al–Mn shape memory alloy. Mater Sci Eng A 800:140386. https://doi.org/10.1016/j.msea.2020.140386

30. Kise S, Araki Y et al (2021) Orientation dependence of plasticity and fracture in single-crystal superelastic Cu–Al–Mn SMA bars. J Mater Civ Eng 33:1–12. https://doi.org/10.1061/(ASCE)MT.1943-5533.0003568

31. Su T, Lu N, Chen C (2021) On the decrease in transformation stress in a bicrystal Cu–Al–Mn shape-memory alloy during cyclic compressive deformation. Materials (Basel) 14:4439. https://doi.org/10.3390/ma14164439

32. Kusama T, Omori T, Saito T et al (2017) Ultra-large single crystals by abnormal grain growth. Nat Commun. https://doi.org/10.1038/s41467-017-00383-0

33. Xu S, Kusama T, Xu X et al (2019) Large [001] single crystals via abnormal grain growth from columnar polycrystal. Materialia 6:100336. https://doi.org/10.1016/j.mtla.2019.100336

34. Yang S, Zhang J, Chi M et al (2019) Excellent superelasticity of Cu–Al–Mn–Cr shape memory single crystal obtained only through annealing cast polycrystalline alloy. Scr Mater 165:20–24. https://doi.org/10.1016/j.scriptamat.2019.02.011

35. Kainuma R (2018) Recent progress in shape memory alloys. Mater Trans 59:327–331. https://doi.org/10.2320/matertrans.M2017340

36. Wang X, Yu J, Liu J et al (2020) Effect of process parameters on the phase transformation behavior and tensile properties of NiTi shape memory alloys fabricated by selective laser melting. Addit Manuf 36:101545. https://doi.org/10.1016/j.addma.2020.101545

37. Rao H, Giet S, Yang K et al (2016) The influence of processing parameters on aluminium alloy A357 manufactured by selective laser melting. Mater Des 109:334–346. https://doi.org/10.1016/j.matdes.2016.07.009

38. Laitinen V, Salminen A, Ullakko K (2019) First investigation on processing parameters for laser powder bed fusion of Ni–Mn–Ga magnetic shape memory alloy. J Laser Appl 31:022303. https://doi.org/10.2351/1.5096108

39. Saedi S, Shayesteh N, Amerinatanzi A et al (2018) On the effects of selective laser melting process parameters on microstructure and thermomechanical response of Ni-rich NiTi. Acta Mater 144:552–560. https://doi.org/10.1016/j.actamat.2017.10.072

40. Carter LN, Martin C, Withers PJ, Attallah MM (2014) The influence of the laser scan strategy on grain structure and cracking behaviour in SLM powder-bed fabricated nickel superalloy. J Alloys Compd 615:338–347. https://doi.org/10.1016/j.jallcom.2014.06.172

41. Marattukalam JJ, Karlsson D, Pacheco V et al (2020) The effect of laser scanning strategies on texture, mechanical properties, and site-specific grain orientation in selective laser melted 316L SS. Mater Des. https://doi.org/10.1016/j.matdes.2020.108852

42. Prasad K, Obana M, Ishii Y et al (2021) The effect of laser scanning strategies on the microstructure, texture and crystallography of grains exhibiting hot cracks in additively manufactured Hastelloy X. Mech Mater 157:103816. https://doi.org/10.1016/j.mechmat.2021.103816

43. Karimi J, Antonov M, Kollo L, Prashanth KG (2022) Role of laser remelting and heat treatment in mechanical and tribological properties of selective laser melted Ti6Al4V alloy. J Alloys Compd 897:163207. https://doi.org/10.1016/j.jallcom.2021.163207

44. Kuai Z, Li Z, Liu B et al (2022) Effects of remelting on the surface morphology, microstructure and mechanical properties of AlSi10Mg alloy fabricated by selective laser melting. Mater Chem Phys 285:125901. https://doi.org/10.1016/j.matchemphys.2022.125901

45. Karimi J, Kollo L, Rahmani R et al (2022) Selective laser melting of in-situ CoCrFeMnNi high entropy alloy: effect of remelting. J Manuf Process 84:55–63. https://doi.org/10.1016/j.jmapro.2022.09.056

46. Liu B, Li BQ, Li Z (2019) Selective laser remelting of an additive layer manufacturing process on AlSi10Mg. Results Phys 12:982–988. https://doi.org/10.1016/j.rinp.2018.12.018

47. Bayati P, Safaei K, Nematollahi M et al (2021) Toward understanding the effect of remelting on the additively manufactured NiTi. Int J Adv Manuf Technol 112:347–360. https://doi.org/10.1007/s00170-020-06378-4

48. Song J, Tang Q, Feng Q et al (2022) Effect of remelting processes on the microstructure and mechanical behaviours of 18Ni-300 maraging steel manufactured by selective laser melting. Mater Charact 184:111648. https://doi.org/10.1016/j.matchar.2021.111648

49. da Silva MR, Gargarella P, Gustmann T et al (2016) Laser surface remelting of a Cu–Al–Ni–Mn shape memory alloy. Mater Sci Eng A 661:61–67. https://doi.org/10.1016/j.msea.2016.03.021

50. Yasa E, Deckers J, Kruth JP (2011) The investigation of the influence of laser re-melting on density, surface quality and microstructure of selective laser melting parts. Rapid Prototyp J 17:312–327. https://doi.org/10.1108/13552541111156450

51. Vaithilingam J, Goodridge RD, Hague RJM et al (2016) The effect of laser remelting on the surface chemistry of Ti6al4V components fabricated by selective laser melting. J Mater Process Technol 232:1–8. https://doi.org/10.1016/j.jmatprotec.2016.01.022

52. Thijs L, Kempen K, Kruth JP, Van Humbeeck J (2013) Fine-structured aluminium products with controllable texture by selective laser melting of pre-alloyed AlSi10Mg powder. Acta Mater 61:1809–1819. https://doi.org/10.1016/j.actamat.2012.11.052

53. Hasanabadi M, Keshavarzkermai A, Asgari H et al (2022) In-situ microstructure control by laser post-exposure treatment during laser powder-bed fusion. SSRN Electron J 4:100110. https://doi.org/10.2139/ssrn.4231789

54. Chmielewska A, Wysocki BA, Gadalińska E et al (2022) Laser powder bed fusion (LPBF) of NiTi alloy using elemental powders: the influence of remelting on printability and microstructure. Rapid Prototyp J 28:1845–1868. https://doi.org/10.1108/RPJ-08-2021-0216

55. Cava RD, Bolfarini C, Kiminami CS et al (2015) Spray forming of Cu-11.85Al-3.2Ni-3Mn (wt.%) shape memory alloy. J Alloys Compd 615:S602–S606. https://doi.org/10.1016/j.jallcom.2013.11.166

56. Gabrysiak K, Gustmann T, Freudenberger J et al (2021) Development and characterization of a metastable Al–Mn–Ce alloy produced by laser powder bed fusion. Addit Manuf Lett 1:100017. https://doi.org/10.1016/j.addlet.2021.100017

57. Hariharan A, Goldberg P, Gustmann T et al (2022) Designing the microstructural constituents of an additively manufactured near β Ti alloy for an enhanced mechanical and corrosion response. Mater Des 217:110618. https://doi.org/10.1016/j.matdes.2022.110618

58. Siddique S, Imran M, Wycisk E et al (2015) Influence of process-induced microstructure and imperfections on mechanical properties of AlSi12 processed by selective laser melting. J Mater Process Technol 221:205–213. https://doi.org/10.1016/j.jmatprotec.2015.02.023

59. Bedmar J, de la Pezuela J, Riquelme A et al (2022) Impact of remelting in the microstructure and corrosion properties of the Ti6Al4V fabricated by selective laser melting. Coatings. https://doi.org/10.3390/coatings12020284

60. Murkute P, Pasebani S, Isgor OB (2019) Production of corrosion-resistant 316L stainless steel clads on carbon steel using powder bed fusion-selective laser melting. J Mater Process Technol 273:116243. https://doi.org/10.1016/j.jmatprotec.2019.05.024

61. Xie J-X, Liu J-L, Huang H-Y (2015) Structure design of high-performance Cu-based shape memory alloys. Rare Met 34:607–624. https://doi.org/10.1007/s12598-015-0557-7

62. Raghavan N, Simunovic S, Dehoff R et al (2017) Localized melt-scan strategy for site specific control of grain size and primary dendrite arm spacing in electron beam additive manufacturing. Acta Mater 140:375–387. https://doi.org/10.1016/j.actamat.2017.08.038

63. Babacan N, Ma J, Turkbas OS et al (2018) The effects of cold rolling and the subsequent heat treatments on the shape memory and the superelasticity characteristics of $Cu_{73}Al_{16}Mn_{11}$ shape memory alloy. Smart Mater Struct 27:015028. https://doi.org/10.1088/1361-665X/aa9cc5

64. La Roca PM, Isola LM, Sobrero CE et al (2015) Grain size effect on the thermal-induced martensitic transformation in polycrystalline Cu-based shape memory alloys. Mater Today Proc 2:S743–S746. https://doi.org/10.1016/j.matpr.2015.07.389

65. Ferretto I, Borzì A, Kim D et al (2022) Control of microstructure and shape memory properties of a Fe–Mn–Si-based shape memory alloy during laser powder bed fusion. Addit Manuf Lett 3:100091. https://doi.org/10.1016/j.addlet.2022.100091

66. Jung HY, Peter NJ, Gärtner E et al (2020) Bulk nanostructured AlCoCrFeMnNi chemically complex alloy synthesized by laser-powder bed fusion. Addit Manuf 35:101337. https://doi.org/10.1016/j.addma.2020.101337

67. Laitinen V, Saren A, Sozinov A, Ullakko K (2022) Giant 5.8% magnetic-field-induced strain in additive manufactured Ni–Mn–Ga magnetic shape memory alloy. Scr Mater 208:114324. https://doi.org/10.1016/j.scriptamat.2021.114324

68. Mallik US, Sampath V (2008) Influence of aluminum and manganese concentration on the shape memory characteristics of Cu–

Al–Mn shape memory alloys. J Alloys Compd 459:142–147. https://doi.org/10.1016/j.jallcom.2007.04.254

69. Morris MA, Lipe T (2014) Microstructural influence of Mn additions on thermoelastic and pseudoelastic properties of Cu–Al–Ni alloys. Acta Metall 42:1583–1594. https://doi.org/10.1016/0956-7151(94)90368-9

70. Sutou Y, Omori T, Kainuma R, Ishida K (2013) Grain size dependence of pseudoelasticity in polycrystalline Cu–Al–Mn-based shape memory sheets. Acta Mater 61:3842–3850. https://doi.org/10.1016/j.actamat.2013.03.022

71. Liu J, Yan W, Li M (2020) Tension-compression asymmetry of superelasticity in unidirectionally solidified Cu–Al–Mn shape memory alloy. J Mater Eng Perform 29:289–295. https://doi.org/10.1007/s11665-020-04588-1

72. Zhuo L, Song B, Li R et al (2020) Effect of element evaporation on the microstructure and properties of CuZnAl shape memory alloys prepared by selective laser melting. Opt Laser Technol 127:106164. https://doi.org/10.1016/j.optlastec.2020.106164